INTERNATIONAL JOURNAL FOR NUMERICAL METHODS IN BIOMEDICAL ENGINEERING
Int. J. Numer. Meth. Biomed. Engng. 2010; **26**:117–138
Published online 12 May 2009 in Wiley InterScience (www.interscience.wiley.com). DOI: 10.1002/cnm.1260

Modelling brain deformations for computer-integrated neurosurgery

K. Miller*, †, A. Wittek, G. Joldes, A. Horton, T. Dutta-Roy, J. Berger and L. Morriss

Intelligent Systems for Medicine Laboratory, School of Mechanical Engineering, The University of Western Australia, 35 Stirling Highway, Crawley, WA 6009, Australia

SUMMARY

In this review paper we discuss Intelligent Systems for Medicine Laboratory's contributions to mathematical and numerical modelling of brain deformation behaviour for neurosurgical simulation and brain image registration. These processes can be reasonably described in purely mechanical terms, such as displacements, strains and stresses and therefore can be analysed using established methods of continuum mechanics. We advocate the use of fully non-linear theory of continuum mechanics. We discuss in some detail modelling geometry, boundary conditions, loading and material properties. We consider numerical problems such as the use of hexahedral and mixed hexahedral–tetrahedral meshes as well as meshless spatial discretization schemes. We advocate the use of total Lagrangian formulation of both finite element and meshless methods together with explicit time-stepping procedures. We support our recommendations and conclusions with two examples: computation of the reaction force acting on a biopsy needle, and computation of the brain shift for image registration. Copyright © 2009 John Wiley & Sons, Ltd.

Received 8 October 2008; Revised 18 March 2009; Accepted 23 March 2009

KEY WORDS: brain; biomechanics; finite element method; meshless methods; surgical simulation; image registration

1. INTRODUCTION

Mathematical modelling and computer simulation have proved tremendously successful in engineering. Computational mechanics has enabled technological developments in virtually every area of our lives. One of the greatest challenges for mechanists is to extend the success of computational mechanics to fields outside traditional engineering, in particular to biology, biomedical sciences, and medicine [1]. By extending the surgeons' ability to plan and carry out surgical interventions more accurately and with less trauma, computer-integrated surgery (CIS) systems could help to improve clinical outcomes and the efficiency of health-care delivery. CIS systems could have a similar impact on surgery to that long since realised in computer-integrated manufacturing (CIM).

In computational sciences, the most critical step in the solution of the problem is the selection of the physical and mathematical model of the phenomenon to be investigated. Model selection is most often a heuristic process, based on the analyst's judgment and experience. Often, model selection is a subjective endeavour; different modellers may choose different models to describe

*Correspondence to: K. Miller, Intelligent Systems for Medicine Laboratory, School of Mechanical Engineering, The University of Western Australia, 35 Stirling Highway, Crawley, WA 6009, Australia.
†E-mail: kmiller@mech.uwa.edu.au

Contract/grant sponsor: Australian Research Council; contract/grant numbers: DP0343112, DP0664534, LX0560460
Contract/grant sponsor: NIH; contract/grant number: 1-RO3-CA126466-01A1

the same reality. Nevertheless, the selection of the model is the single most important step in obtaining valid computer simulations of an investigated reality [1].

In this article we present how various aspects of computer-integrated neurosurgery can benefit from the application of methods of computational mechanics. We discuss physical and mathematical models of the brain deformation behaviour as well as numerical schemes used to solve these models developed in the Intelligent Systems for Medicine Laboratory at the University of Western Australia. We chose to focus on the following two application areas: neurosurgical simulation and neuroimage registration.

1.1. Neurosurgical simulation for operation planning, surgeon training and skill assessment

The goal of surgical simulation research is to model and simulate deformable materials for applications requiring real-time interaction. Medical applications for this include simulation-based training, skills assessment and operation planning.

Surgical simulation systems are required to provide visual and haptic feedback to a surgeon or trainee. Various haptic interfaces for medical simulation are especially useful for training surgeons for minimally invasive procedures (laparoscopy/interventional radiology) and remote surgery using tele-operators. These systems must compute the deformation field within a soft organ and the interaction force between a surgical tool and the tissue to present visual and haptic feedback to the surgeon. Haptic feedback must be provided at frequencies of at least 500 Hz [2]. From a solid-mechanical perspective, the problem involves large deformations, non-linear material properties and non-linear boundary conditions. Moreover, it requires extremely efficient solution algorithms to satisfy stringent requirements on the frequency of haptic feedback. Surgical simulation is a very challenging problem of solid mechanics.

When a simulator is intended to be used for surgeon training, a generic model developed from average organ geometry and material properties can be used in computations. However, when the intended application is for operation planning the computational model must be patient specific. This requirement adds to the difficulty of the problem—the question of how to rapidly generate patient-specific computational models still awaits a satisfactory answer.

1.2. Neuroimage registration (computational radiology)

Examples of new therapeutic technologies that are entering the medical practice now and will be employed in the future include gene therapy, stimulators, focused radiation, lesion generation, nanotechnological devices, drug polymers, robotic surgery and robotic prosthetics [3]. One common element of all these novel therapeutic devices is that they have extremely localised areas of therapeutic effect. As a result, they have to be applied precisely in relation to the patient's current (i.e. intra-operative) anatomy, directly over the specific location of anatomic or functional abnormality [3]. Nakaji and Speltzer [4] list the 'accurate localization of the target' as the first principle in modern neurosurgical approaches.

As only pre-operative anatomy of the patient is known precisely from medical images (usually Magnetic Resonance Images (MRI)), it is now recognised that the ability to predict soft organ deformation (and therefore intra-operative anatomy) during the operation is the main problem in performing reliable surgery on soft organs. We are particularly interested in problems arising in image-guided neurosurgery, see Figure 1. In this context it is very important to be able to predict the effect of procedures on the position of pathologies and critical healthy areas in the brain. If displacements within the brain can be computed during the operation, they can be used to warp pre-operative high-quality MR images so that they represent the current, intra-operative configuration of the brain.

The neuroimage registration problem involves large deformations, non-linear material properties and non-linear boundary conditions as well as the difficult issue of generating patient-specific computational models. However, it is easier than the previously discussed surgical simulation problem in two important ways: we are interested in accurate computations of the displacement field only, accuracy of stress computations is not required; and the computations must be conducted intra-operatively, which practically means that the results should be available to an operating

DOI: 10.1002/cnm

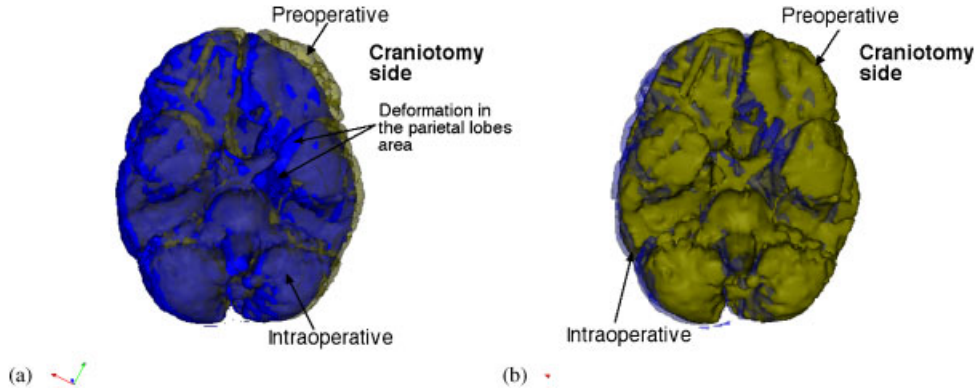

Figure 1. Comparison of the brain surface determined from images acquired pre-operatively with the one determined intra-operatively from the images acquired after craniotomy. Inferior (i.e. 'bottom') view: (a) pre-operative surface is semitransparent. Notice lateral deformation of left parietal lobe surface (shift to the right) and (b) intra-operative surface is semitransparent. Deformation of the brain surface due to craniotomy is clearly visible both near the craniotomy and on the opposite side. Intra-operative displacements of over 20 mm were reported in the medical literature [5]. Surfaces were determined from the images provided by Department of Surgery, Brigham and Women's Hospital (Harvard Medical School, Boston, Massachusetts, U.S.A.).

surgeon in less than 40 s [6–9]. This still forms a stringent requirement for computational efficiency of methods used, but is clearly much easier to satisfy than a 500 Hz haptic feedback frequency requirement for neurosurgical simulation.

Following the Introduction (Section 1), in Section 2 we describe difficulties in modelling geometry, boundary conditions, loading and material properties of the brain. In Section 3 we discuss numerical algorithms devised to efficiently solve brain deformation behaviour models. In Section 4 we consider example applications in the areas of surgical simulation and computational radiology. We conclude with some reflections about the state of the field.

2. BRAIN DEFORMATION BEHAVIOUR—MODELLING ISSUES

2.1. Geometry

Detailed geometric information is needed to define the domain in which the deformation field needs to be computed. Such information is provided by electronic brain atlases [10–13]. In applications that do not require patient-specific data (such as neurosurgical simulators for education and training) the geometric information provided by these atlases is sufficient. However, other applications such as neurosurgical simulators for operation planning and image registration systems require patient-specific data. Such data are available from radiological images (for an example see Figure 2); however, they are significantly inferior in quality to the data available from anatomical atlases. The brain model should contain the brain parenchyma, ventricles and tumour (if present), which needs to be identified in radiological images (in practice MRI).

The accuracy of neurosurgery is not better than 1 mm [3]. Voxel size in high-quality pre-operative MR images is usually of similar magnitude. Therefore, we can conclude that patient-specific models of the brain geometry can be constructed with approximately 1 mm accuracy, and that higher accuracy is probably not required.

A necessary step in the development of the numerical model of the brain is the creation of a computational grid, which in most practical cases is a finite element mesh or a cloud of points required by a meshless method. Because of the stringent computation time requirements, the mesh must be constructed using low-order elements that are not computationally intensive. The linear under-integrated hexahedron is the preferred choice.

DOI: 10.1002/cnm

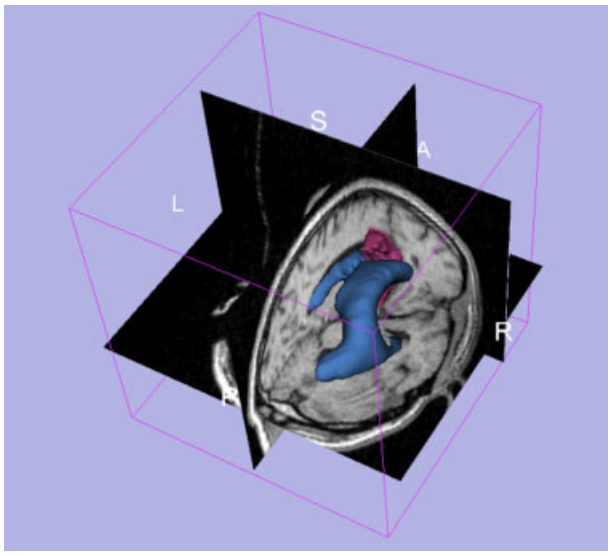

Figure 2. 3D magnetic resonance image presented as a tri-planar cross section. A single slice with clearly visible tumour is shown in Section 4.2, Figure 17(a). Public domain software Slicer (www.slicer.org), developed by our collaborators from Surgical Planning Laboratory, Harvard Medical School, was used to generate the image.

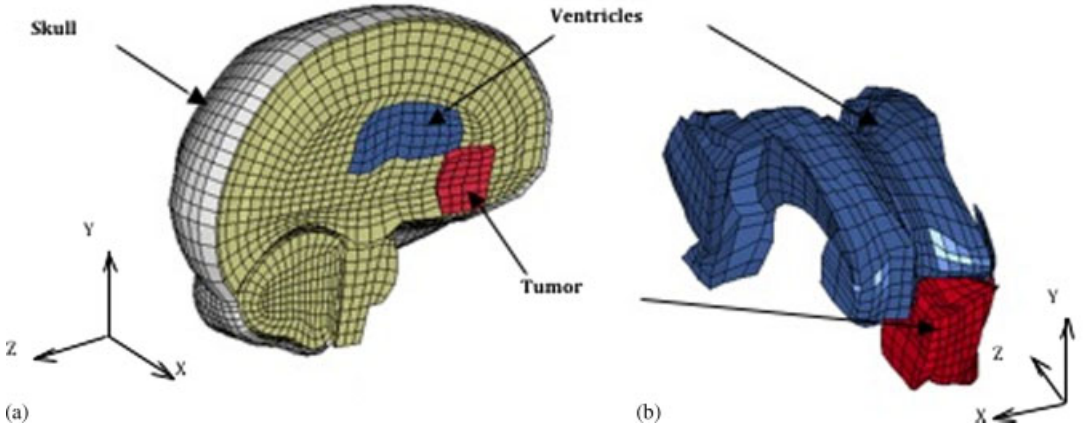

Figure 3. Patient-specific hexahedron-dominant brain mesh [9]. (a) Entire left brain hemisphere and (b) lateral ventricles and tumour. The element characteristic length varied between 0.6 and 6 mm. For 85% of the elements, the characteristic length was between 2 and 4.5 mm.

Many algorithms are now available for fast and accurate automatic mesh generation using tetrahedral elements, but not for automatic hexahedral mesh generation [14–16]. Template-based meshing algorithms can be used for meshing different organs using hexahedrons [17–19], but these types of algorithms only work for healthy organs. In the case of severe pathologies (such as a brain tumour), such algorithms cannot be used, as the shape, size and position of the pathology is unpredictable. This is one reason why many authors proposed the use of tetrahedral meshes for their models [6, 7, 20, 21]. In order to automate the simulation process, mixed meshes having both hexahedral and linear tetrahedral elements are the most convenient, see Figure 3.

An alternative to using the finite element method is to use one of the available meshless methods. The problem of computational grid generation disappears as one needs only to drop a cloud of points into the volume defined by a 3D medical image [22–27], see Figure 4.

DOI: 10.1002/cnm

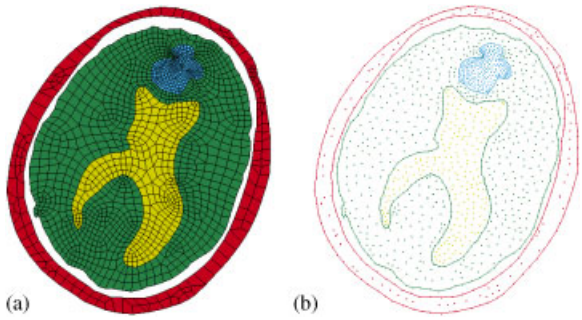

Figure 4. A 2D slice of the brain discretised by: (a) quadrilateral finite elements and (b) nodes of the modified element-free Galerkin method. Development of a good-quality finite element mesh is time consuming. Generation of the meshless grid is almost instantaneous.

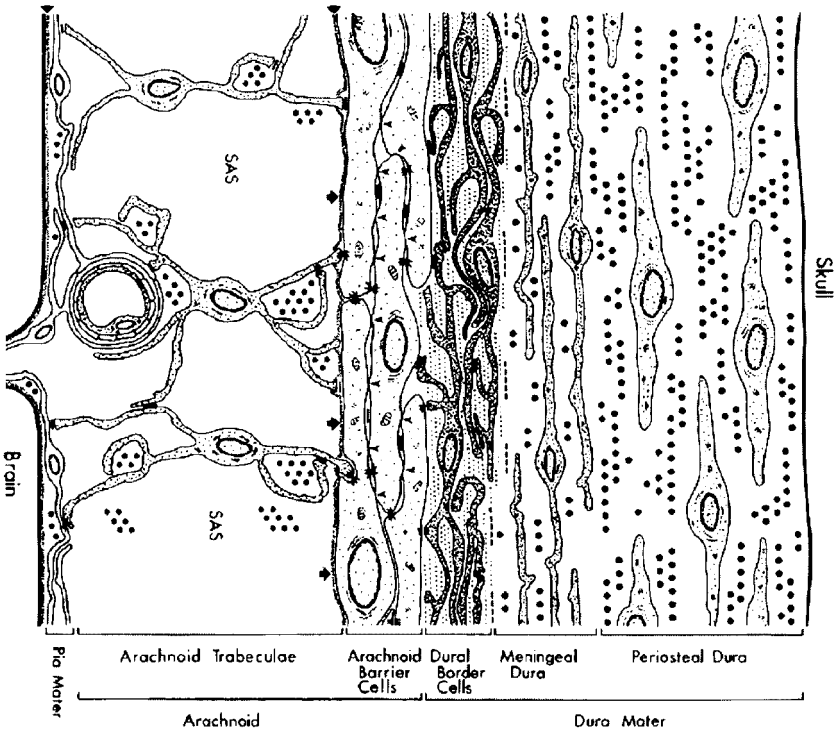

Figure 5. Structure of the brain–skull interface, adapted from [28].

2.2. *Boundary conditions*

The formulation of appropriate boundary conditions for computation of brain deformation constitutes a significant problem because of complexity of the brain–skull interface, see Figure 5.

A number of researchers fix the brain surface to the skull [29, 30]. We do not recommend this approach. Our experience [9, 31–34] and the study by Hu *et al.* [35] suggest that a gap between the brain and the skull which allows for motion of the brain within the cranial cavity is a simple and effective model of the brain–skull interface. Introducing such a gap is consistent with the observation that the brain surface located opposite to craniotomy translates laterally by 2–3 mm (Figure 1). The brain–skull gap thickness needs to be determined from the pre-operative MRIs for each patient considered.

DOI: 10.1002/cnm

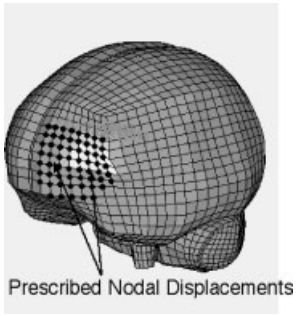

Figure 6. Model loading through prescribed nodal displacements at the exposed brain surface.

As the skull is orders of magnitude stiffer than the brain tissue its rigidity can be assumed. The spine–spinal cord interactions and constraining effects of the spinal cord on the brain rigid body motion can be simulated by constraining the spinal end of the model.

2.3. Loading

We advocate loading the models through imposed displacements on the model surface [9, 33, 36], see Figure 6. In the case of neurosurgical simulation, this loading will be imposed by known motion of a surgical tool. In the case of intra-operative image registration, the current (intra-operative) position of the exposed part of the brain surface can be measured using a variety of techniques [37]. This information can then be used to define model loading.

As suggested in papers [36, 38–40] for problems where loading is prescribed as forced motion of boundaries, the unknown deformation field within the domain depends very weakly on the mechanical properties of the continuum. This feature is of great importance in biomechanical modelling where there are always uncertainties in patient-specific properties of tissues.

2.4. Mechanical properties of brain tissue

Figure 7, adapted from Reference [42], presents a stress–strain relationships for swine brain tissue in compression and extension. The experiments were conducted on cylindrical samples approximately 30 mm in diameter and 13 mm in height.

Experimental results show that the mechanical response of brain tissue to external loading is very complex. The stress–strain relationship is clearly non-linear with no portion in the plots suitable for estimating a meaningful Young's modulus. It is also obvious that the stiffness of the brain in compression is much higher than in extension. The non-linear relationship between stress and strain rate is also apparent. Stresses at moderately high strain rate ($0.64\,\mathrm{s}^{-1}$) are about ten times higher than at the low strain rate of $0.64\,\mathrm{s}^{-1} \times 10^{-5}\,\mathrm{s}^{-1}$. These results are in general agreement with measurements conducted by groups from the University of Sydney [43, 44], University of Pennsylvania [45, 46] and Eindhoven University of Technology [47].

To account for such complicated mechanical behaviour we proposed the Ogden-based hyper-viscoelastic constitutive model of the following form [42, 48]:

$$W = \frac{2}{\alpha^2}\int_0^t \left[\mu(t-\tau)\frac{\mathrm{d}}{\mathrm{d}\tau}(\lambda_1^\alpha + \lambda_2^\alpha + \lambda_3^\alpha - 3)\right]\mathrm{d}\tau \tag{1}$$

$$\mu = \mu_0\left[1 - \sum_{k=1}^{n} g_k(1 - \mathrm{e}^{-t/\tau_k})\right] \tag{2}$$

where W is the strain energy, λ_1, λ_2, λ_3 are principal extensions, α is a material coefficient without physical meaning. We identified the value of α to be -4.7, see Table I. t and τ denote time. Equation (2) describes viscous response of the tissue. μ_0 is the instantaneous shear modulus in the undeformed state. τ_k are characteristic relaxation times.

DOI: 10.1002/cnm

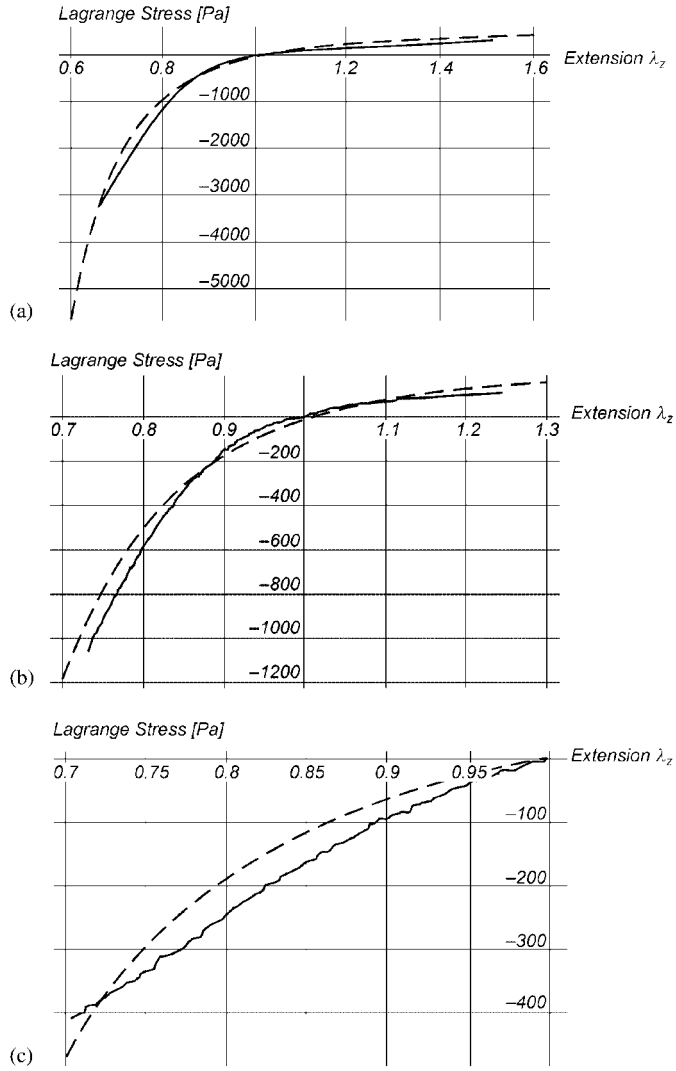

Figure 7. Experimental (solid line) versus theoretical (dashed line, Equations (1) and (2) and Table I) results for uniaxial compression [41] and extension [42] of brain tissue for various loading velocities. For this simple experimental configuration, Lagrange stress (vertical axis) is the vertical force divided by the undeformed cross-sectional area, and extension (horizontal axis) is the current height divided by the initial height, i.e. extension less than one indicates compression. Negative values of stress indicate compression: (a) loading velocity $v = 5.0 \times 10^2$ mm/min; corresponding to the strain rate approx. $0.64\,s^{-1}$; (b) loading velocity $v = 5.0$ mm/min; corresponding to the strain rate approx. $0.64\,s^{-1} \times 10^{-2}\,s^{-1}$; (c) loading velocity $v = 5.0 \times 10^{-3}$ mm/min; corresponding to the strain rate approx. $0.64\,s^{-1} \times 10^{-5}\,s^{-1}$ (compression only).

Table I. List of material constants for the constitutive model of brain tissue, Equations (1) and (2), $n = 2$ [42].

Instantaneous response	$k = 1$	$k = 2$
$\mu_0 = 842$ Pa $a = -4.7$	Characteristic time $t_1 = 0.5$ s $g_1 = 0.450$	Characteristic time $t_2 = 50$ s $g_2 = 0.365$

DOI: 10.1002/cnm

The material constants (identified from experiment) are given in Table I. One-dimensional response, as predicted by Equations (1) and (2), is shown in Figure 7.

One advantage of the proposed model is that the implementation of the constitutive equation presented here is already available in commercial finite element software [49–51] and can be used immediately for large-scale computations.

It is important to examine the simplifying assumptions behind the model described by Equations (1) and (2), and Table I: *incompressibility* and *isotropy*.

1. *Incompressibility*. Very soft tissues are most often assumed to be incompressible, see e.g. [52–58]. In experiments on brain tissue at moderate strain rates we have not detected a departure from this assumption [59].
2. *Isotropy* (*i.e. mechanical properties are assumed to be the same in all directions*). Very soft tissues do not normally bear mechanical loads and do not exhibit directional structure (provided that a large enough sample is considered: for the brain we used samples of 30 mm diameter and 13 mm height). Therefore, they may be assumed to be initially isotropic, see e.g. [42, 44, 52, 58, 60–64].

Prange and Margulies [46] reported anisotropic properties of brain tissue; however, their sample sizes were 1 mm wide. At such a small scale, the fibrous nature of most tissues will cause detectable difference in directional properties. Experiments discussed here were aimed at identifying 'average' properties at the length scales relevant to surgical procedures. At such scales, brain tissue can be safely assumed to exhibit no directional variation of mechanical properties.

Average properties, such as those described above, are not sufficient for patient-specific computations of stresses and reaction forces because of the very large variability inherent to biological materials. This is clearly demonstrated in the biomechanics literature, see e.g. [42, 43, 46, 48]. Unfortunately, despite recent progress in elastography using ultrasound [65] and MR [66, 67], reliable methods of measuring patient-specific properties of the brain are not yet available.

3. SOLUTION ALGORITHMS

When designing a finite element solution method there are many aspects that must be considered, such as the formulation used (total or updated Lagrangian), type of elements used for constructing the mesh or density and placement of nodes and integration points in meshless methods, as well as time-integration scheme. We will discuss these aspects in this section.

3.1. Integration of the equations of continuum mechanics

The algorithms implemented in the great majority of commercial finite element programs use the updated Lagrangian formulation, where all variables are referred to the current (i.e. from the end of the previous time step) configuration of the system (ABAQUS [49], LS-DYNA [50], Ansys [68], ADINA [69], etc.). The advantage of this approach is the simplicity of incremental strain description and low internal memory requirements. The disadvantage is that all derivatives with respect to spatial coordinates must be recomputed in each time step, because the reference configuration is changing.

The internal memory cost is no longer a prohibitive factor so that in developing our finite element algorithms we used the total Lagrangian formulation, where all variables are referred to the original configuration of the system. The decisive advantage of this formulation is that all derivatives with respect to spatial coordinates are calculated relative to the original configuration and therefore can be pre-computed—this is particularly important for time-critical applications such as surgical simulation and intra-operative image registration.

Because biological tissue behaviour can be described in general using hyper-elastic or hyper-viscoelastic models, such as that given in Equations (1) and (2), the use of the total Lagrangian formulation also leads to a simplification of material law implementation as these material models can be easily described using the deformation gradient.

DOI: 10.1002/cnm

The integration of equilibrium equations in the time domain can be done using either implicit or explicit methods [70–72]. The most commonly used implicit integration methods, such as Newmark's constant acceleration method, are unconditionally stable. This implies that their time step is limited only by the accuracy considerations. However, the implicit methods require solution of a set of non-linear algebraic equations at each time step. Furthermore, iterations need to be performed for each time step of implicit integration to control the error and prevent divergence. Therefore, the number of numerical operations per each time step can be three orders of magnitude larger than for explicit integration [70].

On the other hand, in explicit methods, such as the central difference method, treatment of non-linearities is very straightforward and no iterations are required. By using a lumped (diagonal) mass matrix [70], the equations of motion can be decoupled and no system of equations must be solved. Computations are done at the element or support domain level eliminating the need for assembling the stiffness matrix of the entire model. Thus, the computational cost of each time step and internal memory requirements is substantially smaller for explicit than for implicit integration. There is no need for iterations anywhere in the algorithm. These features make explicit integration suitable for real-time applications.

However, the explicit methods are only conditionally stable. Normally, a severe restriction on the time-step size has to be included in order to receive satisfactory simulation results. Stiffness of soft tissues is very low [42, 48, 62, 73], e.g. stiffness of the brain is about eight orders of magnitude lower than that of common engineering materials such as steel. Since the maximum time step allowed for stability is (roughly speaking) inversely proportional to the square root of Young's modulus divided by the mass density [50], it is possible to conduct simulations of brain deformation with much longer time steps than in typical dynamic simulations in engineering. This was confirmed in our previous simulations of brain shift using the commercial finite element solver LS-DYNA [9, 32]. Therefore, when developing the suite of finite element algorithms for the computation of brain tissue deformation, we combined total Lagrange formulation with explicit time integration.

A detailed description of the total Lagrange explicit dynamics (TLED) algorithm is presented in [74]. The main benefits of the TLED algorithm are:

- allows pre-computing of many variables involved (e.g. derivatives with respect to spatial coordinates and hourglass control parameters);
- no accumulation of errors—increase stability for quasi-static solutions;
- easy implementation of the material law for hyper-elastic materials using the deformation gradient;
- straightforward treatment of non-linearities;
- no iterations required for a time step;
- no system of equations needs to be solved;
- low computational cost for each time step.

3.2. Computational grid: elements used in the finite element mesh

3.2.1. 8-noded under-integrated hexahedron with hourglass control. The under-integrated hexahedral elements require the use of an hourglass control algorithm in order to eliminate the instabilities, known as zero energy modes, which arise from the single-point integration [75]. One of the most popular and powerful hourglass control algorithms, which is currently available in many commercial software finite element packages, is the one proposed in [75]. This method is applicable for hexahedral and quadrilateral elements with arbitrary geometry undergoing large deformations.

Starting from the algorithm proposed by Flanagan and Belytschko we showed that the total Lagrangian formulation is advantageous from the point of view of efficient hourglass control implementation, as many quantities involved can be pre-computed. We have shown in [76] that the hourglass control forces for each element can be computed (in matrix form) as

$$ {}^{t}_{0}\mathbf{F}^{\mathrm{Hg}} = k_0 \boldsymbol{\gamma}_0 \boldsymbol{\gamma}^{\mathrm{T}} {}^{t}_{0}\mathbf{u} \tag{3} $$

DOI: 10.1002/cnm

where k is a constant which depends on the element geometry and material properties, $\boldsymbol{\gamma}$ is the matrix of hourglass shape vectors and $\mathbf{u}$ is the matrix of current displacements. The notation from [71] is used, where the left superscript represents the current time and the left subscript represents the time of the reference configuration, which is 0 for total Lagrangian formulation. In Equation (3) all quantities except $\mathbf{u}$ are constant and can be pre-computed, making the hourglass control mechanism very efficient from the computational point of view.

3.2.2. Non-locking tetrahedral elements. As fast generation of good-quality hexahedral meshes for objects with complicated geometry is not yet possible, we must be prepared to have a substantial number of tetrahedral elements in the mesh. For example, using software IA-FE Mesh (http://www.ccad.uiowa.edu/mimx/IA-FEMesh/), recently developed by researchers from The University of Iowa [77], one can generate a purely hexahedral mesh of the brain. However, this mesh contains a substantial number of highly distorted elements that are very difficult to correct and in practice must be replaced by tetrahedra (or a meshless grid).

In modelling of incompressible continua, artificial stiffening (often referred to as volumetric locking) affects many standard elements including the linear tetrahedral element, see e.g. [78]. This phenomenon occurs also for nearly incompressible materials and therefore introducing slight compressibility does not solve the problem.

A number of improved linear tetrahedral elements with anti-locking features have been proposed by different authors [79–82]. The average nodal pressure (ANP) tetrahedral element proposed in [79] is computationally inexpensive and provides much better results for nearly incompressible materials compared with the standard tetrahedral element. Nevertheless, one shortcoming of the ANP element and its implementation in a finite element code is the handling of interfaces between different materials. We extended the formulation of the ANP element so that all elements in a mesh are treated in the same way, requiring no special handling of the interface elements [83].

In our implementation the ANP element only modifies the deviatoric component of the strain energy of the standard tetrahedral element, which in turn depends only on the volumetric part of the deformation gradient. Therefore, we can obtain the desired behaviour of the ANP element by modifying the volumetric part of the deformation gradient of the standard tetrahedral element (the element Jacobian).

Because the element Jacobian is equal to the determinant of the element deformation gradient, we define a modified deformation gradient that has the same isochoric part as the normal deformation gradient, but the volumetric part is modified so that its determinant (and therefore the volumetric deformation) is equal to the element Jacobian required by the ANP element:

$$\bar{\mathbf{X}}^{(e)} = (\bar{J}^{(e)})^{1/3}(J^{(e)})^{-1/3}\mathbf{X}, \quad J^{(e)} = \det(\mathbf{X}) \tag{4}$$

The computation of the nodal forces (or stiffness matrix) can now be done in the usual manner, but using the modified deformation gradient instead of the normal deformation gradient for defining the strains. This way any existing material law implementation can be used.

3.3. Meshless computational grid

The use of meshless methods is motivated by simple, automatic computational grid generation for patient-specific simulations. We use a modified element-free Galerkin method [24] that is meshless in the sense that deformation is calculated at nodes that are not part of an element mesh. Node placement is almost arbitrary. Volumetric integration is performed over a regular background grid that does not conform to the simulation geometry. Geometrically, non-linear total Lagrangian formulation is used together with explicit time integration via the central difference method, which makes our meshless algorithm in many respects similar to the TLED algorithm discussed in Section 3.1.

Support domain and moving least-squares theory deal with the relationship between integration points and nodes. The theory was initially developed by Lancaster and Salkauskas [84] and used for meshless methods in the diffuse element method and element-free Galerkin in [25, 85].

For shape functions, we use moving least squares in our algorithm for simplicity and robustness. Figure 8 depicts the spherical support domain of the node x^*. The n blackened nodes belong to the

DOI: 10.1002/cnm

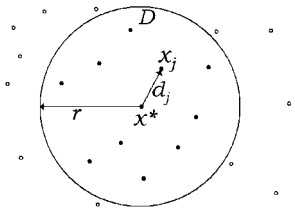

Figure 8. Node x^* with its neighbourhood D.

support domain of node x^*. After calculating the moving least-squares shape functions of a given integration point in the pre-processing stage, we only use the $3n$ first partial spatial derivatives in the remainder of our simulation.

The computational efficiency of this meshless algorithm is dependent mostly on the number of integration points where stresses need to be evaluated. For the same number of nodes our algorithm requires approximately twice as many integration points as a finite element mesh composed of under-integrated hexahedra. However, the algorithm requires only between half and one third as many integration points as a tetrahedral-dominant mesh. Therefore, our algorithm is significantly faster than the TLED-based finite element method using tetrahedral finite elements.

Typical problems that arise from using our meshless method include poor approximations of free boundaries and instability from either disjoint support domains or singular shape functions. These problems are common for other meshless methods known from the literature as well.

3.4. Modelling of interaction between the brain and the skull: contact algorithm

Many simulations require the treatment of interactions between different parts of the model. In order to handle the brain–skull interaction we developed a very efficient algorithm that treats this interaction as a finite sliding, frictionless contact between a deformable object (the brain) and a rigid surface (the skull) [86]. Unlike contacts in commercial finite element solvers (e.g. ABAQUS, LS-DYNA), our contact algorithm has no configuration parameters (as it only imposes kinematic restrictions on the movement of the brain surface nodes) and is very fast, with the speed almost independent of the mesh density for the skull surface.

The main parts of the contact algorithm are: detection of nodes on the brain surface (also called the slave surface), which has penetrated the skull surface (master surface) and the displacement of each slave node that has penetrated the master surface to the closest point on the master surface.

The surfaces of the anatomical structures of segmented brain images are typically discretised using triangles; therefore, we consider the skull surface as a triangular mesh. We will call each triangle surface as 'face', the vertices—'nodes' and the triangle sides—'edges'.

We base our penetration detection algorithm on the closest master node (nearest neighbour) approach [50]. The basic algorithm is as follows: For each slave node P:

- Find the closest master node C (global search).
- Check the faces and edges surrounding C for penetration (local search).

To improve the computation speed, following [50], we implemented the global search phase using bucket sort. A good description of this searching algorithm is given in [87]. In our implementation the size of the buckets used for the global search is different in the three directions, being given in each direction by half of the maximum size of the projections of all master edges on that direction. This ensures that the number of nodes in each bucket is minimal while there are no cases in which a closest node cannot be found.

The next step (local search) aims at finding for each slave node P, the closest node R (on the master surface) on the faces or edges surrounding node C. Once the closest point on the master surface is identified, the penetration is detected by checking the sign of the scalar product $RP \cdot \mathbf{n}$, with $\mathbf{n}$ the inside normal to the master surface in R. For an edge or a node the normal is defined as the sum of the normal vectors of adjacent faces.

DOI: 10.1002/cnm

In most of the cases, the basic tests presented above are sufficient for identifying the closest point on the master surface. Nevertheless, there are also special cases that must be considered, when the closest point on the master surface is not on the faces and edges adjacent to C. In commercial software, this problem is solved by searching for the closest face or edge on the master surface instead of searching for the closest master node [50]. This search is time consuming even if bucket sort is used. Therefore, our proposal for handling these special cases is to conduct an analysis of the master surface and identify for each node C all the faces and edges that can be penetrated by a slave node P in the case C is the closest master node to P. A detailed description of this analysis is presented in [86]. The identified faces and edges are kept in a list for each master node C and are checked in addition to the faces and edges that contain C when the local search is performed. Because the master surface is rigid this analysis can be done pre-operatively, greatly reducing the contact computation time during the intra-operative simulation.

3.5. Verification of the developed algorithms

The accuracy and reliability of new algorithms are best assessed against existing, verified numerical procedures implemented in commercial finite element packages. Validation by modelling of an actual surgery may be compromised by many unknowns (e.g. patient-specific geometry, boundary conditions and material properties) involved in such a simulation. Here, we present comparison of the results obtained with finite element algorithms presented in this section and results obtained with ABAQUS [49] for brain indentation.

The main focus of the brain indentation simulation was to verify the developed algorithms in terms of their accuracy in predicting reaction forces. The mesh we used had 2428 nodes and 2059 elements (2023 under-integrated hexahedron and 36 improved tetrahedral elements in the indentation area—see Figure 9).

The indentation was simulated by displacing four nodes in the direction normal to the brain surface by 20 mm using a smooth loading curve. An almost incompressible neo-Hookean material was used for the brain tissue (mass density of 1000 kg/m^3, Young's modulus in un-deformed state equal to 3000 Pa and Poisson's ratio 0.49) and a compressible neo-Hookean material for the ventricle (mass density of 1000 kg/m^3, Young's modulus in un-deformed state equal to 100 Pa and Poisson's ratio 0.1). The same constraints as in [88] were used and brain symmetry was assumed.

In ABAQUS we used fully integrated mixed formulation elements for the mesh, which are the 'gold standard' elements in case of almost incompressible materials simulations [49]. We used the implicit solver with the default configuration.

Computations were performed on a standard 3 GHz Intel® Core™ Duo CPU system using Windows XP operating system. The simulation consisted of 2000 time steps and took less than 2 s using our TLED method, allowing for a force feedback frequency of about 1000 Hz. The ABAQUS implicit simulation performed 100 time steps in about 3 min. There is very good agreement between the results obtained using our software and the results from the ABAQUS simulation, in cases of

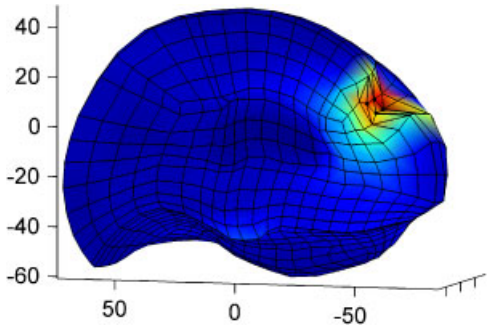

Figure 9. Simulation of brain indentation—the mixed mesh is deformed by displacing four nodes. Dimensions are in mm.

DOI: 10.1002/cnm

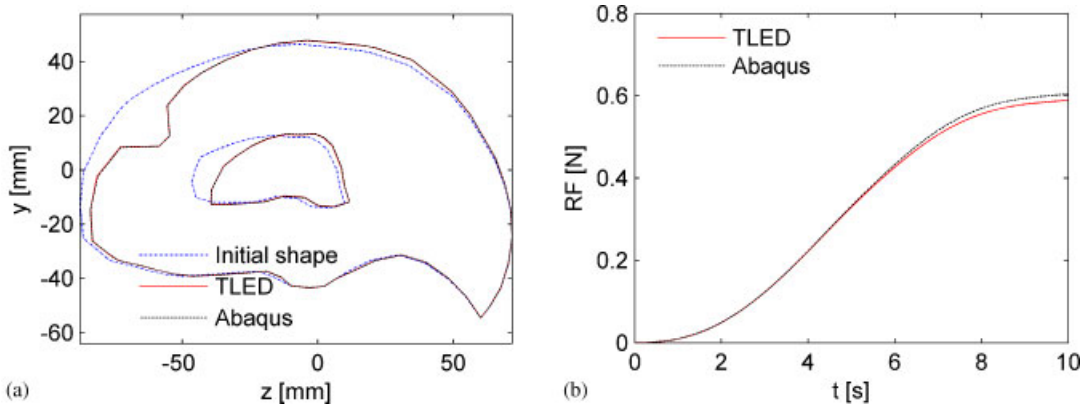

Figure 10. Computed displacements (a) and reaction forces (b) using ABAQUS implicit solver and our algorithms.

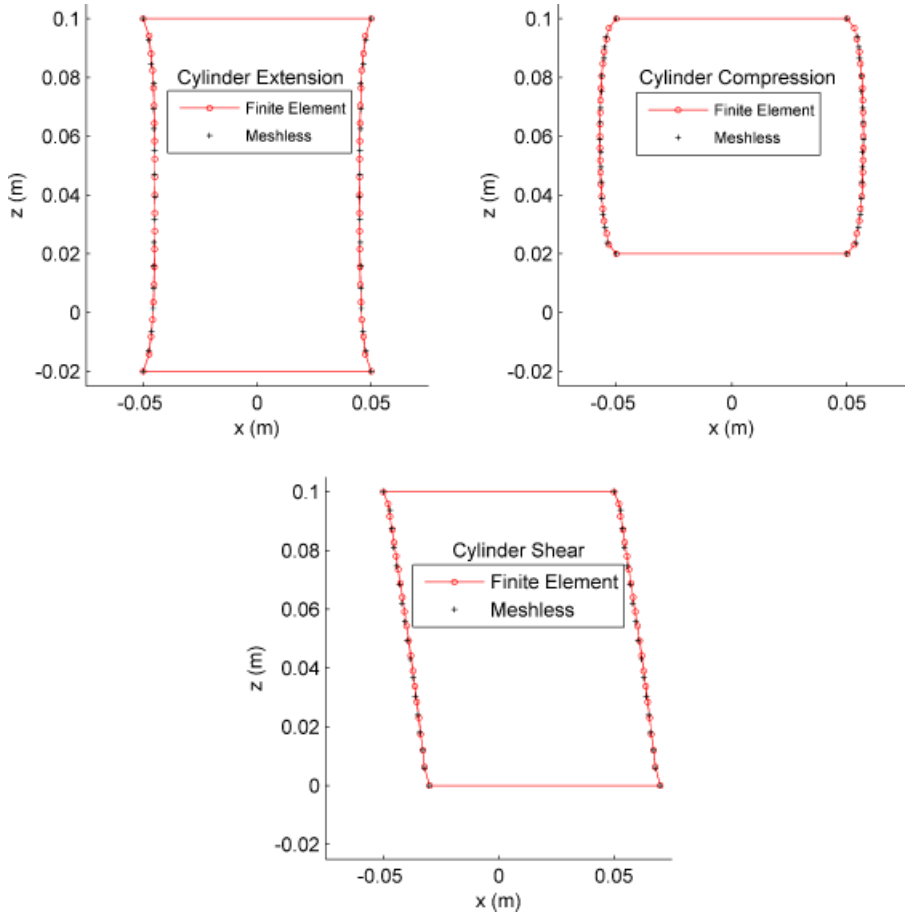

Figure 11. Extension, compression and shear of a cylinder.

both displacements and reaction forces (Figure 10)—the displaced profiles overlap almost exactly and the maximum relative error in reaction forces is 2.5%.

Verification of the meshless algorithm was conducted using compression, extension and shear of a cylinder, and indentation of an ellipsoid [23, 89]. The computed reaction forces differ by less

DOI: 10.1002/cnm

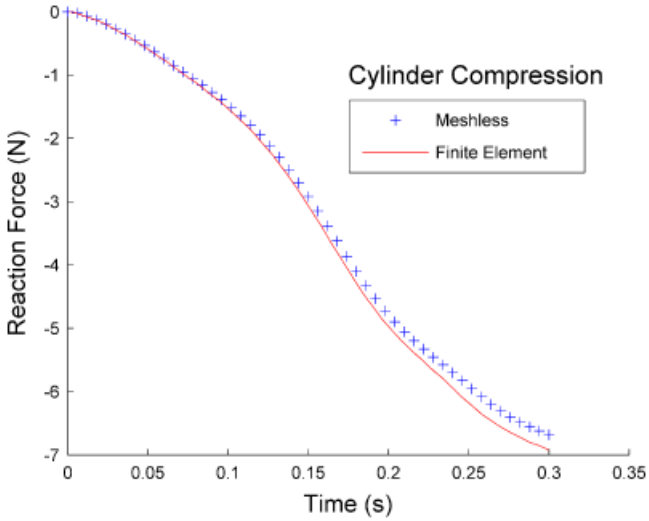

Figure 12. Reaction force for compression of a cylinder as computed using ABAQUS fully integrated, mixed formulation hexahedrons and our meshless method.

than 1%, and the displacements by less than 0.15 mm from those computed with fully integrated mixed formulation ABAQUS elements, see Figures 11 and 12.

4. APPLICATION EXAMPLES

4.1. Modelling the brain for neurosurgical simulation—computer simulation of needle insertion

Previous models for predicting forces acting on a needle during insertion into very soft organs (such as the brain) relied on oversimplifying assumptions of infinitesimal deformations, linear elastic constitutive models and specific experimentally derived functions for determining needle—tissue interactions [2, 90, 91]. In [92] we proposed a more general approach in which the needle forces are determined directly from the equations of continuum mechanics using fully non-linear finite element procedures that account for large deformations (geometric non-linearity) and non-linear stress–strain relationship (material non-linearity) of soft tissues. We applied these procedures to model needle insertion into a swine brain using the constitutive properties determined from the experiments on tissue samples obtained from the same brain (i.e. the subject-specific constitutive properties were used). We focused on the insertion phase preceding puncture of the brain meninges and obtained an accurate prediction of the needle force. This demonstrates the utility of non-linear finite element procedures in patient-specific modelling of needle insertion into soft organs such as, e.g. brain. The experiment designed to validate our computations is shown in Figure 13.

The brain mesh consisting of 19 337 hexahedra (Figure 14) was constructed from the MRIs of a swine. The details of mesh construction are given in [92].

In order to accurately model the needle–brain interactions, the element size when discretizing the brain should be close to the needle tip diameter. As this diameter was 0.55 mm, over a million elements would be required to discretise the entire swine brain. This would result in an extremely long computation time. Therefore, only a graft of dimensions of $6\times6\times12$ mm in the direct neighbourhood of the needle insertion point was discretised using elements of size of 0.5–1 mm. Elements of size of up to 3.5 mm were used for the remaining part of the brain (Figure 14).

Pia mater is a membrane surrounding the brain. It was discretised using 4401 shell elements rigidly attached (through node sharing) to the hexahedral elements forming the outer layer of the brain. Belytschko–Tsay shell elements [93] with one integration point across the thickness were used, i.e. these elements had no bending stiffness.

DOI: 10.1002/cnm

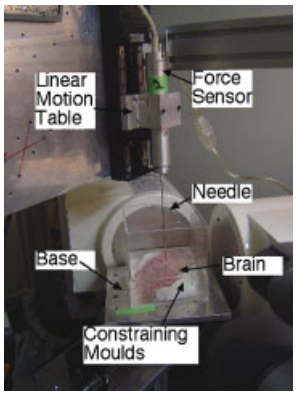

Figure 13. Needle insertion into swine brain: experimental set-up.

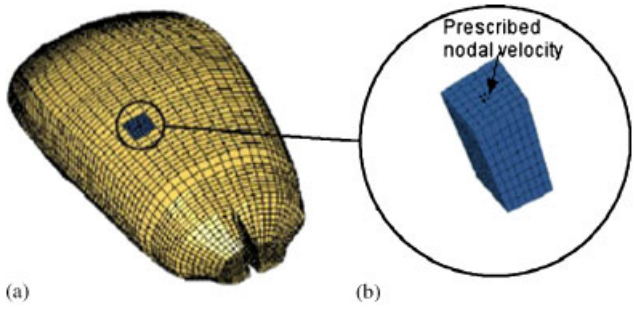

Figure 14. (a) General view of the swine brain mesh developed in this study and (b) refined mesh graft in the needle insertion area.

The brain model was loaded through the prescribed motion of four nodes located in the area that was in contact with the needle during the actual insertion (Figure 15). The sum of forces at these nodes was a close approximation of the reaction force between the brain and the needle. A constant velocity of $5\,\mathrm{mm\,s^{-1}}$ was used when prescribing the nodal motion. The motion was applied for 2.0 s, which corresponds to needle insertion depth (i.e. the needle displacement measured from the start of contact between the needle and pia mater) of 10 mm. This depth was selected as the experiments on needle insertion indicated that the needle punctures the pia mater when the insertion depth reaches 7–10 mm. Our finite element model summarised in Figure 14 predicted accurately the force–displacement relationship obtained experimentally when inserting the needle into the swine brain (Figure 15).

For needle displacement of up to 7 mm, the predicted force–displacement relationship was close to the average relationship obtained from all the needle insertions conducted in this study (i.e. 18 insertions into three brains) (Figure 15). This indicates consistency in our experimental and modelling results.

Although the pia mater puncture was not modelled in this study, our biomechanical model of needle insertion makes it possible to predict the strain field in pia mater and brain at the instant the pia mater punctures. Such prediction can be done in the following way. From the experimental needle force–displacement curves, one can determine the needle displacement at which the puncture occurred. Then the strain corresponding to this displacement can be predicted using the model. In this study, the pia puncture occurred at the needle displacement of 7–10 mm (measured from the start of contact between the needle and pia mater surface). The model summarised in Figure 14 predicted that in the needle insertion area, the pia mater Almansi effective strain was 65% at the displacement of 7 mm, and 90% at the displacement of 10 mm. The Almansi maximum principal strain was 60 and 80% at the displacement of 7 and 10 mm, respectively.

DOI: 10.1002/cnm

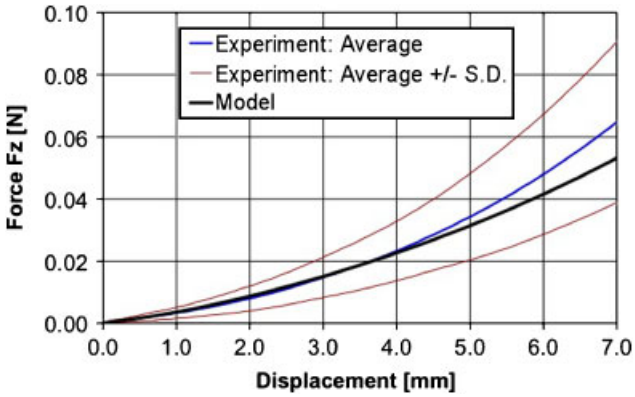

Figure 15. Needle insertion into the swine brain. Experimental corridor (average +/− standard deviation S.D.) of force–displacement relationship (18 insertions) and the relationship predicted using the finite element model. The experimental curves were cut at the instant pia mater punctured, i.e. only the results prior to the puncture are shown.

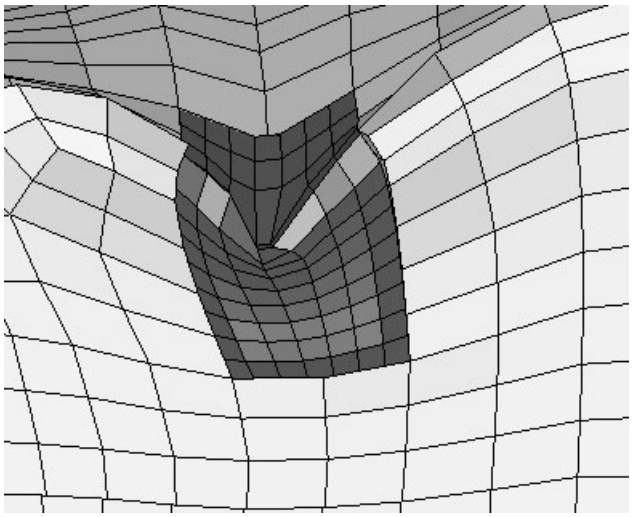

Figure 16. Modelling of needle insertion into the swine brain. The model cross section at the needle displacement is 10 mm.

Thus, our model predicted very large local strains and deformations in the needle insertion area, which is visualised in Figure 16. Geometric non-linearity of the analysed problem is evident from this figure. Therefore, it is very unlikely that any model in which infinitesimal deformations are assumed (as in the case of linear elasticity) would produce reliable results when applied to simulation of needle insertion into brain.

We obtained very similar results using our meshless total Lagrangian algorithm [24].

4.2. Modelling the brain for image registration—computer simulation of the brain shift

A particularly exciting application of non-rigid image registration is in intra-operative image-guided procedures, where high-resolution pre-operative scans are warped onto sparse intra-operative ones [8, 94]. We are particularly interested in registering high-resolution pre-operative MRI with lower-quality intra-operative imaging modalities, such as multi-planar MRI and intra-operative ultrasound. To achieve accurate matching of these modalities, accurate and fast algorithms to compute tissue deformations are fundamental.

DOI: 10.1002/cnm

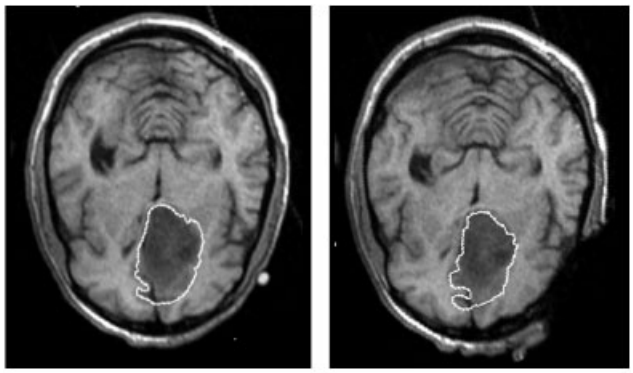

(a) (b)

Figure 17. (a) Pre- and (b) intra-operative MRIs of the head. The tumour segmentation is indicated by white lines in the anterior brain part. 3D view of the pre-operative MR volume is shown in Figure 2.

Table II. Observed and computed centres of gravity displacements for ventricles and tumour. x, y and z directions are as in Figure 3.

	Ventricles			Tumor		
Material model	ΔX	ΔY	ΔZ	ΔX	ΔY	ΔZ
Center of gravity displacements (mm)						
MRI determined	3.4	0.2	1.7	5.5	−0.2	1.7
Hyper-viscoelastic material	2.6	−0.1	2.1	5.2	−0.4	2.7
Hyper-elastic material	2.6	−0.1	2.1	5.2	−0.4	2.7
Linear elastic material	2.6	−0.1	2.1	5.0	−0.5	2.7

During the craniotomy, gravity acceleration acted in the xz plane and formed a 24.5° angle with the z axis.

Here, we present examples of computational results of brain shift, taken from [9, 33, 95]. For this case the craniotomy-induced displacement of the tumour, as observed on intra-operative MR images, was about 6 mm, Figure 1. Patient-specific geometry was used. The pre- and intra-operative positions of the tumour are shown in Figure 17. The finite element mesh is given in Figure 3. The results are given in Table II and Figures 18 and 19.

The computed craniotomy-induced displacements of the tumour and ventricles' centre of gravity (COG) agreed well with the actual ones determined from the radiographic images (Table II). With the exception of the tumour COG displacement along the inferior–superior axis, the differences between the computed and observed displacements were below 0.8 mm. An important (and not unexpected) feature of the results summarised in Table II is that the displacements of the tumour and ventricle COGs differ appreciably. This feature can be explained only by the fact that the brain undergoes both local deformation and global rigid body motion (i.e. the whole brain moves), which justifies the use of non-rigid registration. It is worth noting here that linear elasticity theory (commonly used by the medical image analysis community) is not capable of describing the deformation field that is a superposition of rigid body motion and local displacements.

Detailed comparison of cross sections of the actual tumour and ventricle surfaces acquired intra-operatively with the ones predicted by the present brain model, indicates that although some local miss-registration is visible, particularly in the inferior tumour part (Figures 18 and 19), the result is remarkably good.

It is worth noting that as the model was loaded by the enforced motion of the exposed part of the surface of the brain, the resulting displacement field is almost insensitive to mechanical properties of brain tissue, see Table II. This is an important result that allows using biomechanical models for intra-operative image registration without knowing precisely patient-specific properties of the tissue [33].

DOI: 10.1002/cnm

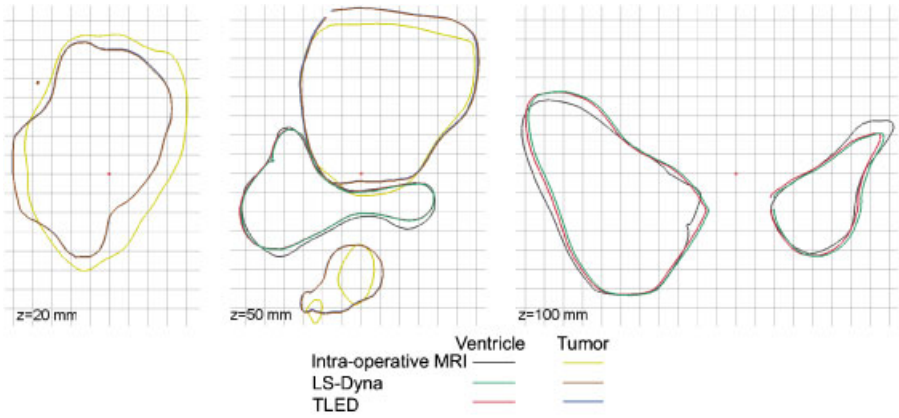

Figure 18. Comparison of contours of coronal sections of ventricles and tumour obtained from the intra-operative images with the ones predicted using the brain model. Positions of section cuts are measured from the most anterior point of the frontal cortex (posterior direction is positive).

Figure 19. Comparison of contours of axial sections of ventricles and tumour obtained from the intra-operative images with the ones predicted using the brain model. Positions of section cuts are measured from the most superior point of the parietal cortex (superior direction is positive).

State-of-the-art image analysis methods, such as those based on optical flow [96, 97], mutual information-based similarity [98, 99], entropy-based alignment [100] and block matching [101, 102]), work perfectly well when the differences between the images to be co-registered are not too large. It can be expected that the non-linear biomechanics-based model supplemented by appropriately chosen image analysis methods would provide a reliable method for brain image registration in a clinical setting.

5. CONCLUSIONS

Computational mechanics has become a central enabling discipline that has led to greater understanding and advances in modern science and technology [1]. It is now in a position to make

DOI: 10.1002/cnm

a similar impact in medicine. We have discussed modelling approaches of two applications of clinical relevance: surgical simulation and neuroimage registration. These problems can be reasonably characterised with the use of purely mechanical terms such as displacements, internal forces, etc. Therefore, they can be analysed using the methods of continuum mechanics. Moreover, similar methods may find applications in modelling the development of structural diseases of the brain [34, 89, 103, 104].

As the brain undergoes large displacements ($\sim 10-20$ mm in the case of a brain shift) and its mechanical response to external loading is strongly non-linear, we advocate the use of general, non-linear finite element procedures for the numerical solution of the proposed models.

The brain's complicated mechanical behaviour: non-linear stress–strain and stress–strain rate relationships, and much lower stiffness in extension than in compression, require very careful selection of the constitutive model for a given application. The selection of the constitutive model for surgical simulation problems depends on the characteristic strain rate of the process to be modelled and to a certain extent on computational efficiency considerations. Fortunately, as shown in Section 4.2 and [33] the precise knowledge of patient-specific mechanical properties of brain tissue is not required for intra-operative image registration.

A number of challenges must be met before CIS systems based on computational biomechanical models can become as widely used as CIM systems are now. As we deal with individual patients, methods to produce patient-specific computational grids quickly and reliably must be improved. Substantial progress in automatic meshing methods is required, or alternatively meshless methods may provide a solution. Computational efficiency is an important issue, as intra-operative applications, requiring reliable results within approximately 40 s, are most appealing. Progress can be made in non-linear algorithms by identifying parts that can be pre-computed, and parts that do not have to be calculated at every time step. Use of the total Lagrangian formulation of the finite element method [71, 105, 106], where all field variables are related to the original (known) configuration of the system and therefore most spatial derivatives can be calculated before the simulation commences, during the pre-processing stage offers such a possibility. Implementation of algorithms in parallel on networks of processors, and harnessing the computational power of graphics processing units provides a challenge for coming years.

ACKNOWLEDGEMENTS

The financial support of the Australian Research Council (Grants No. DP0343112, DP0664534 and LX0560460) and NIH (Grant No. 1-RO3-CA126466-01A1) is gratefully acknowledged. We thank our collaborators Dr Ron Kikinis and Dr Simon Warfield from the Harvard Medical School, and Dr Kiyoyuki Chinzei and Dr Toshikatsu Washio from the Surgical Assist Technology Group of AIST, Japan for help in various aspects of our work. The medical images used in the present study (provided by Dr Simon Warfield) were obtained in the investigation supported by a research grant from the Whitaker Foundation. We thank Toyota Central R&D Labs. (Nagakute, Aichi, Japan) for providing the THUMS brain model.

REFERENCES

1. Oden JT *et al.* Research directions in computational mechanics. *Computer Methods in Applied Mechanics and Engineering* 2003; **192**:913–922.
2. DiMaio SP, Salcudean SE. Interactive simulation of needle insertion models. *IEEE Transactions on Biomedical Engineering* 2005; **52**(7):1167–1179.
3. Bucholz R, MacNeil W, McDurmont L. The operating room of the future. *Clinical Neurosurgery* 2004; **51**: 228–237.
4. Nakaji P, Speltzer RF. The marriage of technique, technology, and judgement. *Innovations in Surgical Approach* 2004; **51**:177–185.
5. Roberts DW *et al.* Intraoperative brain shift and deformation: a quantitative analysis of cortical displacement in 28 cases. *Neurosurgery* 1998; **43**:749–758.
6. Ferrant M *et al.* Serial registration of intraoperative MR images of the brain. *Medical Image Analysis* 2002; **6**(4):337–359.
7. Warfield SK *et al.* Real-time registration of volumetric brain MRI by biomechanical simulation of deformation during image guided surgery. *Computing and Visualization in Science* 2002; **5**:3–11.

DOI: 10.1002/cnm

8. Warfield SK *et al.* Capturing intraoperative deformations: research experience at Brigham and womens's hospital. *Medical Image Analysis* 2005; **9**(2):145–162.
9. Wittek A *et al.* Patient-specific model of brain deformation: application to medical image registration. *Journal of Biomechanics* 2007; **40**:919–929.
10. Kikinis R *et al.* A digital brain atlas for surgical planning, model driven segmentation and teaching. *IEEE Transactions on Visualization and Computer Graphics* 1996; **2**(3):232–241.
11. Nowinski WL. From research to clinical practice: a Cerefy brain atlas story. *International Congress Series* 2003; **1256**:75–81.
12. Nowinski WL, Benabid AL. New directions in atlas-assisted stereotactic functional neurosurgery. In *Advanced Techniques in Image-Guided Brain and Spine Surgery*, IM G (ed.). Thieme: New York, 2002; 162–174.
13. Nowinski WL, Thirunavuukarasuu A, Benabid AL. *The Cerefy Clinical Brain Atlas*. Thieme: New York, 2003.
14. Owen SJ. A survey of unstructured mesh generation technology. *Seventh International Meshing Roundtable*, Dearborn, MI, U.S.A., 1998.
15. Viceconti M, Taddei F. Automatic generation of finite element meshes from computed tomography data. *Critical Reviews in Biomedical Engineering* 2003; **31**(1):27–72.
16. Owen SJ. Hex-dominant mesh generation using 3D constrained triangulation. *Computer-Aided Design* 2001; **33**:211–220.
17. Castellano-Smith AD *et al.* Constructing patient specific models for correcting intraoperative brain deformation. *Fourth International Conference on Medical Image Computing and Computer Assisted Intervention* (*MICCAI*), Lecture Notes in Computer Science, vol. 2208, Utrecht, The Netherlands, 2001.
18. Couteau B, Payan Y, Lavallée S. The mesh-matching algorithm: an automatic 3D mesh generator for finite element structures. *Journal of Biomechanics* 2000; **33**:1005–1009.
19. Luboz V *et al.* Orbital and maxillofacial computer aided surgery: patient-specific finite element models to predict surgical outcomes. *Computer Methods in Biomechanics and Biomedical Engineering* 2005; **8**(4):259–265.
20. Ferrant M *et al.* Deformable modeling for characterizing biomedical shape changes. *Discrete Geometry for Computer Imagery*: *9th International Conference*, Uppsala, Sweden. Springer: Berlin, 2000.
21. Clatz O *et al.* Patient specific biomechanical model of the brain: application to Parkinson's disease procedure. *International Symposium on Surgery Simulation and Soft Tissue Modeling* (*IS4TM'03*), Juan-les-Pins, France. Springer: Berlin, 2003.
22. Horton A, Wittek A, Miller K. Computer simulation of brain shift using an element free Galerkin method. *Seventh International Symposium on Computer Methods in Biomechanics and Biomedical Engineering* (*CMBEE*) *2006*, Antibes, France, 2006.
23. Horton A, Wittek A, Miller K. Towards meshless methods for surgical simulation. *Computational Biomechanics for Medicine Workshop*, *Medical Image Computing and Computer-Assisted Intervention* (*MICCAI*) *2006*, Copenhagen, Denmark, 2006.
24. Horton A, Wittek A, Miller K. Subject-specific biomechanical simulation of brain indentation using a meshless method. *International Conference on Medical Image Computing and Computer-Assisted Intervention* (*MICCAI*) *2007*, Brisbane, Australia. Springer: Berlin, 2007.
25. Belytschko T, Lu YY, Gu L. Element-free Galerkin methods. *International Journal for Numerical Methods in Engineering* 1994; **37**:229–256.
26. Liu GR. *Mesh Free Methods*: *Moving Beyond the Finite Element Method*. CRC Press: Boca Raton, 2003.
27. Li S, Liu WK. *Meshfree Particle Methods*. Springer: Berlin, 2004.
28. Haines DE, Harkey HL, Al-Mefty O. The 'subdural' space: a new look at an outdated concept. *Neurosurgery* 1993; **32**:111–120.
29. Hagemann A *et al.* Biomechanical modeling of the human head for physically based, nonrigid image registration. *IEEE Transactions on Medical Imaging—Special Issue on Model-Based Analysis of Medical Images* 1999; **18**(10):875–884.
30. Miga MI *et al.* In vivo quantification of a homogenous brain deformation model for updating preoperative images during surgery. *IEEE Transactions on Biomedical Engineering* 2000; **47**(2):266–273.
31. Wittek A, Omori K. Parametric study of effects of brain-skull boundary conditions and brain material properties on responses of simplified finite element brain model under angular acceleration in sagittal plane. *JSME International Journal* 2003; **46**(4):1388–1398.
32. Wittek A *et al.* Brain shift computation using a fully nonlinear biomechanical model. *Eighth International Conference on Medical Image Computing and Computer Assisted Surgery* (*MICCAI*) *2005*, Palm Springs, CA, U.S.A., 2005.
33. Wittek A, Hawkins T, Miller K. On the unimportance of constitutive models in computing brain deformation for image-guided surgery. *Biomechanics and Modeling in Mechanobiology* 2009; **8**(1):77–84.
34. Dutta-Roy T, Wittek A, Miller K. Biomechanical modelling of normal pressure hydrocephalus. *Journal of Biomechanics* 2008; **41**(10):2263–2271.
35. Hu J *et al.* Intraoperative brain shift prediction using a 3D inhomogeneous patient-specific finite element model. *Journal of Neurosurgery* 2007; **106**:164–169.
36. Miller K, Wittek A. Neuroimage registration as displacement—zero traction problem of solid mechanics. *Computational Biomechanics for Medicine MICCAI-associated Workshop*. MICCAI: Copenhagen, 2006.
37. Miga MI *et al.* Cortical surface registration for image-guided neurosurgery using laser-range scanning. *IEEE Transactions on Medical Imaging* 2003; **22**(8):973–985.

DOI: 10.1002/cnm

38. Miller K. Method of testing very soft biological tissues in compression. *Journal of Biomechanics* 2005; **38**: 153–158.
39. Miller K. Biomechanics without mechanics: calculating soft tissue deformation without differential equations of equilibrium. *Fifth Symposium on Computer Methods in Biomechanics and Biomedical Engineering* (*CMBBE2004*). First Numerics: Madrid, Spain, 2005.
40. Miller K. How to test very soft biological tissues in extension. *Journal of Biomechanics* 2001; **34**(5):651–657.
41. Miller K, Chinzei K. Constitutive modeling of brain tissue: experiment and theory. *Journal of Biomechanics* 1997; **30**(11–12):1115–1121.
42. Miller K, Chinzei K. Mechanical properties of brain tissue in tension. *Journal of Biomechanics* 2002; **35**:483–490.
43. Bilston LE, Liu Z, Phan-Tien N. Linear viscoelastic properties of bovine brain tissue in shear. *Biorheology* 1997; **34**(6):377–385.
44. Bilston L, Liu Z, Phan-Tiem N. Large strain behaviour of brain tissue in shear: some experimental data and differential constitutive model. *Biorheology* 2001; **38**:335–345.
45. Thibault KL, Margulies SS. Age-dependent material properties of the porcine cerebrum: effect on pediatric inertial head injury criteria. *Journal of Biomechanics* 1998; **31**:1119–1126.
46. Prange MT, Margulies SS. Regional, directional, and age-dependent properties of the brain undergoing large deformation. *ASME Journal of Biomechanical Engineering* 2002; **124**:244–252.
47. Brands DWA, Peters GWM, Bovendeerd PHM. Design and numerical implementation of a 3-D non-linear viscoelastic constitutive model for brain tissue during impact. *Journal of Biomechanics* 2004; **37**(1):127–134.
48. Miller K. *Biomechanics of Brain for Computer Integrated Surgery*. Publishing House of Warsaw University of Technology: Warsaw, 2002.
49. ABAQUS I. *ABAQUS Online Documentation*: *Version 6.5-1*, 2004.
50. Hallquist JO. *LS-DYNA Theory Manual*. Livermore Software Technology Corporation: Livermore, CA, 2005.
51. LS-DYNA. *Keyword User's Manual. Version 970*. Livermore Software Technology Corporation: Livermore, CA, 2003.
52. Walsh EK, Schettini A. Calculation of brain elastic parameters in vivo. *American Journal of Physiology* 1984; **247**:R637–R700.
53. Estes MS, McElhaney JH. Response of brain tissue of compressive loading. *ASME Paper No. 70-BHF-13*, 1970.
54. Pamidi MR, Advani SH. Nonlinear constitutive relations for human brain tissue. *Transactions of ASME*, *Journal of Biomechanical Engineering* 1978; **100**:44–48.
55. Sahay KB *et al.* Elastomechanical characterization of brain tissues. *Journal of Biomechanics* 1992; **25**:319–326.
56. Ruan JS, Khalil T, King AI. Dynamic response of the human head to impact by three-dimensional finite element analysis. *Journal of Biomechanical Engineering* 1994; **116**(February):44–50.
57. Voo L *et al.* Finite-element models of the human head. *Medical and Biological Engineering and Computing* 1996; **34**:375–381.
58. Miller K. Constitutive model of brain tissue suitable for finite element analysis of surgical procedures. *Journal of Biomechanics* 1999; **32**:531–537.
59. Miller K, Chinzei K. Compression of swine brain tissue: experiment in vitro. *Journal of Mechanical Engineering Laboratory* 1996; **50**(4):106–115.
60. Mendis KK, Stalnaker RL, Advani SH. A constitutive relationship for large deformation finite element modeling of brain tissue. *Journal of Biomechanical Engineering* 1995; **117**:279–285.
61. Miller K. Constitutive modelling of abdominal organs. *Journal of Biomechanics* 2000; **33**:367–373.
62. Miller K *et al.* Mechanical properties of brain tissue in-vivo: experiment and computer simulation. *Journal of Biomechanics* 2000; **33**:1369–1376.
63. Nasseri S, Bilston LE, Phan-Thien N. Viscoelastic properties of pig kidney in shear, experimental results and modelling. *Rheologica Acta* 2002; **41**:180–192.
64. Farshad M *et al.* Material characterization of the pig kidney in relation with the biomechanical analysis of renal trauma. *Journal of Biomechanics* 1999; **32**(4):417–425.
65. Salcudean S, Turgay E, Rohling R. Identifying the mechanical properties of tissue by ultrasound strain imaging. *Ultrasound in Medicine and Biology* 2006; **32**(2):21–35.
66. Sinkus R *et al.* Viscoelastic shear properties of in vivo breast lesions measured by MR elastography. *Magnetic Resonance Imaging* 2005; **23**:159–165.
67. McCracken J *et al.* Mechanical transient-based magnetic resonance elastography. *Magnetic Resonance in Medicine* 2005; **53**(3):628–639.
68. ANSYS. *ANSYS Home Page*. Available from: www.ansys.com.
69. ADINA R&D. *ADINA Home Page*. Available from: www.adina.com [cited 28/03/2008].
70. Belytschko T. A survey of numerical methods and computer programs for dynamic structural analysis. *Nuclear Engineering and Design* 1976; **37**:23–34.
71. Bathe K-J. *Finite Element Procedures*. Prentice-Hall: Englewood Cliffs, NJ, 1996.
72. Crisfield MA. Non-linear dynamics. *Non-linear Finite Element Analysis of Solids and Structures*. Wiley: Chichester, 1998; 447–489.
73. Miller K, Chinzei K. Constitutive modelling of brain tissue: experiment and theory. *Journal of Biomechanics* 1997; **30**(11–12):1115–1121.
74. Miller K *et al.* Total Lagrangian explicit dynamics finite element algorithm for computing soft tissue deformation. *Communications in Numerical Methods in Engineering* 2007; **23**:121–134.

DOI: 10.1002/cnm

75. Flanagan DP, Belytschko T. A uniform strain hexahedron and quadrilateral with orthogonal hourglass control. *International Journal for Numerical Methods in Engineering* 1981; **17**:679–706.
76. Joldes GR, Wittek A, Miller K. An efficient hourglass control implementation for the uniform strain hexahedron using the total Lagrangian formulation. *Communications in Numerical Methods in Engineering* 2007; DOI:10.1002/cnm.1034.
77. Magnotta VA, Li W, Grosland NM. Comparison of displacement-based and force-based mapped meshing. *Computational Biomechanics for Medicine III MICCAI-Associated Workshop*. MICCAI: New York, 2008.
78. Hughes TJR. *The Finite Element Method*: *Linear Static and Dynamic Finite Element Analysis*. Dover Publications: Mineola, 2000; 682.
79. Bonet J, Burton AJ. A simple averaged nodal pressure tetrahedral element for incompressible and nearly incompressible dynamic explicit applications. *Communications in Numerical Methods in Engineering* 1998; **14**:437–449.
80. Bonet J, Marriott H, Hassan O. An averaged nodal deformation gradient linear tetrahedral element for large strain explicit dynamic applications. *Communications in Numerical Methods in Engineering* 2001; **17**:551–561.
81. Zienkiewicz OC *et al.* Triangles and tetrahedra in explicit dynamic codes for solids. *International Journal for Numerical Methods in Engineering* 1998; **43**:565–583.
82. Dohrmann CR *et al.* Node-based uniform strain elements for three-node triangular and four-node tetrahedral meshes. *International Journal for Numerical Methods in Engineering* 2000; **47**:1549–1568.
83. Joldes GR, Wittek A, Miller K. Non-locking tetrahedral finite element for surgical simulation. *Communications in Numerical Methods in Engineering* 2008; DOI:10.1002/cnm.1185.
84. Lancaster P, Salkauskas K. Surfaces generated by moving least squares methods. *Mathematics of Computation* 1981; **37**(155):141–158.
85. Nayroles B, Touzot G, Villon P. Generalizing the finite element method: diffuse approximation and diffuse elements. *Computational Mechanics* 1992; **10**(5):307–318.
86. Joldes GR *et al.* Realistic and efficient brain-skull interaction model for brain shift computation. *Computational Biomechanics for Medicine III Workshop*. MICCAI: New York, 2008.
87. Sauve RG, Morandin GD. Simulation of contact in finite deformation problems—algorithm and modelling issues. *International Journal of Mechanics and Materials in Design* 2004; **1**:287–316.
88. Wittek A *et al.* Computing reaction forces on surgical tools for robotic neurosurgery and surgical simulation. *Australasian Conference on Robotics and Automation* (*ACRA*), Canberra, Australia, 2004.
89. Berger J *et al.* Coupling finite element and mesh-free methods for modelling brain deformations in response to tumour growth. *Computational Biomechanics for Medicine III MICCAI-Associated Workshop*. MICCAI: New York, 2008.
90. DiMaio S, Salcudean SE. Needle insertion modeling and simulation. *IEEE Transactions on Robotics and Automation* 2003; **19**(5):864–875.
91. Okamura AM, Simone C, O'Leary MD. Force modeling for needle insertion into soft tissue. *IEEE Transactions on Biomedical Engineering* 2004; **51**(10):1707–1716.
92. Wittek A *et al.* Subject-specific non-linear biomechanical model of needle insertion into the brain. *Computer Methods in Biomechanics and Biomedical Engineering* 2007; **11**(2):135–146.
93. Belytschko T, Tsay CS. Explicit algorithms for non-linear dynamics of shells. *Computational Methods in Applied Mechanical Engineering* 1984; **42**:225–251.
94. Ferrant M *et al.* Registration of 3-D intraoperative MR images of the brain using a finite-element biomechanical model. *IEEE Transactions on Medical Imaging* 2001; **20**:1384–1397.
95. Wittek A *et al.* Computation of the brain shift using a non-linear biomechanical model. *Eighth International Conference on Medical Image Computing and Computer Assisted Intervention*, Palm Springs, CA, U.S.A., 2005.
96. Beauchemin SS, Barron JL. The computation of optical flow. *ACM Computing Surveys* 1995; **27**:433–467.
97. Horn BKP, Schunk BG. Determining optical flow. *Artificial Intelligence* 1981; **17**:185–203.
98. Wells III, William M *et al.* Multi-modal volume registration by maximization of mutual information. *Medical Image Analysis* 1996; **1**(1):35–51.
99. Viola P. *Alignment by Maximization of Mutual Information*, Artificial Intelligence Laboratory, Massachusetts Institute of Technology, 1995.
100. Warfield SK *et al.* A binary entropy measure to assess nonrigid registration algorithms. *Fourth International Conference on Medical Image Computing and Computer-Assisted Intervention MICCAI*, Utrecht, The Netherlands, 2001.
101. Dengler J, Schmidt M. The dynamic pyramid—a model for motion analysis with controlled continuity. *International Journal of Pattern Recognition and Artificial Intelligence* 1988; **2**:275–286.
102. Rosenfeld A, Kak AC. Digital picture processing. *Computer Science and Applied Mathematics*. Academic Press: New York, 1976.
103. Taylor Z, Miller K. Reassessment of brain elasticity for analysis of biomechanisms of hydrocephalus. *Journal of Biomechanics* 2004; **37**:1263–1269.
104. Miller K, Taylor Z, Nowinski WL. Towards computing brain deformations for diagnosis, prognosis and nerosurgical simulation. *Journal of Mechanics in Medicine and Biology* 2005; **5**(1):105–121.
105. Miller K *et al.* Total Lagrangian explicit dynamics finite element algorithm for computing soft tissue deformation. *Communications in Numerical Methods in Engineering* 2007; **23**(2):121–134.
106. Zienkiewicz OC, Taylor RL. *The Finite Element Method*. McGraw-Hill: London, 2000.